# Orthotopic Bone Regeneration within 3D Printed Bioceramic Scaffolds with Region-Dependent Porosity Gradients in an Equine Model

Paweena Diloksumpan, Rafael Vindas Bolaños, Stefan Cokelaere, Behdad Pouran, Janny de Grauw, Mattie van Rijen, René van Weeren, Riccardo Levato,* and Jos Malda*

The clinical translation of three-dimensionally printed bioceramic scaffolds with tailored architectures holds great promise toward the regeneration of bone to heal critical-size defects. Herein, the long-term in vivo performance of printed hydrogel-ceramic composites made of methacrylated-oligocaprolactone-poloxamer and low-temperature self-setting calcium-phosphates is assessed in a large animal model. Scaffolds printed with different internal architectures, displaying either a designed porosity gradient or a constant pore distribution, are implanted in equine tuber coxae critical size defects. Bone ingrowth is challenged and facilitated only from one direction via encasing the bioceramic in a polycaprolactone shell. After 7 months, total new bone volume and scaffold degradation are significantly greater in structures with constant porosity. Interestingly, gradient scaffolds show lower extent of remodeling and regeneration even in areas having the same porosity as the constant scaffolds. Low regeneration in distal regions from the interface with native bone impairs ossification in proximal regions of the construct, suggesting that anisotropic architectures modulate the cross-talk between distant cells within critical-size defects. The study provides key information on how engineered architectural patterns impact osteoregeneration in vivo, and also indicates the equine tuber coxae as promising orthotopic model for studying materials stimulating bone formation.

## 1. Introduction

In the quest for methods to heal large bone defects, bioceramic-based scaffolds can overcome current key challenges, such as limited donor material availability or donor site morbidity that are associated with the use of allografts and autografts. Since their composition mimics that of the inorganic phase of the native bone and because of their proven osteoconductivity, bioceramics based on calcium phosphates (CaP) have been extensively evaluated as conduits to guide bone regeneration.[1] Focus during the last decades has been on how properties like solubility, particle size, crystallinity, surface roughness, and surface charge of CaP-based implants may affect their bioactivity and interaction with host tissue. Clearly, both chemical and physical properties of these implants may, by themselves or through their interactions, affect the rate and quality of new tissue formation.[2]

The influence of scaffold porosity on the regenerative process has also been a major topic of investigation.[3,4] Recent studies have highlighted how the pore size, shape, and interconnections are essential in driving the exchange of nutrients and bone remodeling, cellular and vascular

P. Diloksumpan, S. Cokelaere, Dr. J. de Grauw, Prof. R. van Weeren, Dr. R. Levato, Prof. J. Malda
Department of Clinical Sciences
Faculty of Veterinary Medicine
Utrecht University
Yalelaan 1, Utrecht 3584 CL, The Netherlands
E-mail: r.levato-2@umcutrecht.nl; j.malda@umcutrecht.nl

Dr. R. V. Bolaños
Escuela de Medicina Veterinaria
Universidad Nacional Costa Rica
Barreal de Heredia Heredia, Lagunilla 86-3000, Costa Rica

Dr. B. Pouran, M. van Rijen, Dr. R. Levato, Prof. J. Malda
Department of Orthopaedics and Regenerative Medicine Center
University Medical Center Utrecht
Utrecht University
Heidelberglaan 100, Utrecht 3584 CX, The Netherlands

infiltration, progenitor cell differentiation, material degradation, and immunological response.[5,6] Although specific pore features, such as size, geometry, and directionality, can to a certain extent be controlled with conventional scaffold fabrication techniques, recent developments in additive manufacturing (AM) technologies have greatly enhanced the capacity of designing and fine-tuning the specific scaffold architecture.

An anisotropic pore distribution can, for example, be introduced in printed structures to mimic the native gradient from highly porous cancellous bone to less porous cortical bone in the subchondral bone layer in implants for osteochondral repair in articulating joints.[7,8] However, even though a pore size of over 300 µm has often been recommended for facilitating bone and vascular ingrowth within porous scaffolds,[9] the in vivo performance of anisotropic yet geometrically defined porous printed ceramic implants has not been fully explored.

Recently, low-temperature self-setting CaP cements based on alpha-tricalcium phosphate ($\alpha$-TCP) microparticles, which are also used as injectable bone cements,[10] have emerged as promising materials for printable ceramic formulations. In fact, by accurately controlling the rheology of the cement precursor paste, these cements can be utilized as a biomaterial ink[11] for extrusion-based 3D printing. After printing, the printed structure is exposed to a humidified environment at physiological temperature to initiate the setting reaction by converting the $\alpha$-TCP paste into calcium deficient hydroxyapatite cement (CDHA). This is a mild reaction that permits co-printing of such CaP cements with cell-laden bioinks to generate composite constructs.[12] This class of materials has already been successfully exploited to obtain printed CaP cements with osteoinductive properties, either by encapsulation of growth factors in the paste precursor[13] or by tuning printable CaP nano-topography.[14] As new three-dimensionally (3D) printed CDHA-based scaffolds with controllable macro- and microscale architectures are becoming available, it becomes increasingly important to investigate their relative regenerative potential not only in vitro, but also in reliable animal models.[15,16]

In orthopedic regenerative medicine, the evaluation of novel interventions in large animal models is a pre-requisite for their eventual human clinical application. However, at the same time, such human pre-clinical studies constitute end-stage testing for veterinary application in the animal species involved.[17–19] Much like humans and unlike other more common large animal models like goats or sheep, horses participate as athletes in competitions, in which bone and osteochondral injuries regularly lead to both great economic losses and serious animal welfare concerns.[20–22] This makes studies addressing bone regenerative capacity in the horse not only of great interest for human medicine, but also for the equestrian industry and equine health care.[18,19]

This study aimed at the evaluation of the in vivo bone regenerative potential of a novel CaP-based scaffold with a variation in pore distribution in an equine model. Low temperature setting CaP-based bioceramic-hydrogel composite scaffolds, consisting of ($\alpha$-TCP), hydroxyapatite nanoparticles (nano-HA), and a biodegradable, crosslinkable poloxamer derivative were fabricated via 3D printing, to create scaffolds with either an isotropic pore distribution or a anisotropic gradient of porosity. Finally, to better assess the ability of bone to grow within large constructs,

the regenerative process was challenged by encasing the CaP scaffold within a polycaprolactone (PCL) cage, which prevented infiltration of progenitor cells from the periosteum and allowed preferentially unidirectional tissue ingrowth. The scaffolds were implanted orthotopically in the tuber coxae of horses and bone regeneration was studied over a 7-month period.

## 2. Results and Bone Regeneration within 3D Printed Bioceramic

### 2.1. Implants and Postoperative Clinical Data

The implants consisted of printable hydrogel-calcium phosphate ceramic composite scaffolds (PCaP) encased within a non-porous PCL chamber, as detailed in the experimental section. Scaffolds were produced to obtain constructs characterized either by a discrete gradient or constant pore distribution in the direction of layer-by-layer deposition of the printable material (z-direction) (**Figure 1**). The gradient scaffolds were characterized by four regions with decreasing distances between the PCaP strands (500, 400, 300, and 200 µm), whereas the constant scaffolds displayed consistently a 500 µm fiber spacing. Total porosities of the fabricated scaffolds were 40.03 ± 1.78% and 51.14 ± 0.78% for the gradient and constant architectures, respectively. Both types of scaffolds were implanted at the tuber coxae of each horse by randomly transplanting each type of scaffold in each side (1 defect/side) (**Figure 2**). After 7 months, the surgical incisions healed without complications, and no local inflammatory reactions (heat, swelling, tenderness) or signs of pain or discomfort were observed at any time. Likewise, the animals did not experience any detectable pain or lameness during the postoperative period, the rehabilitation period, or other parts during the course of the experiment. Clinical and blood parameters remained within the normal physiologic limits (Table S1, Supporting Information). Only in one case, partial wound dehiscence occurred during the recovery period, and after re-suturing, the wound healed without further complications and the correct positioning of the implant at the defect site was confirmed by radiography. At the time of euthanasia, surgical sites were easily identified, both visually and by palpation. In some cases a slight depression was observed at the site of the defects; in others there was some thickening because of scar tissue formation. After removal of the overlying soft tissues, the implants appeared all well attached to the surrounding osseous tissue. There were no signs of any inflammation or otherwise adverse reactions.

### 2.2. Quantitative Analyses

Upon retrieval of the implants at the end point of the experiment, four scaffolds per group could be safely used for the analysis of the effect of the porous architecture on osteoregeneration and displayed a structurally integer PCL cage, as observed via micro computed tomography (µCT) (Figure S1, Supporting Information). First of all, our data confirm that the material and the printed scaffolds produced with it have high potential to guide bone regeneration. Among the structures in which the
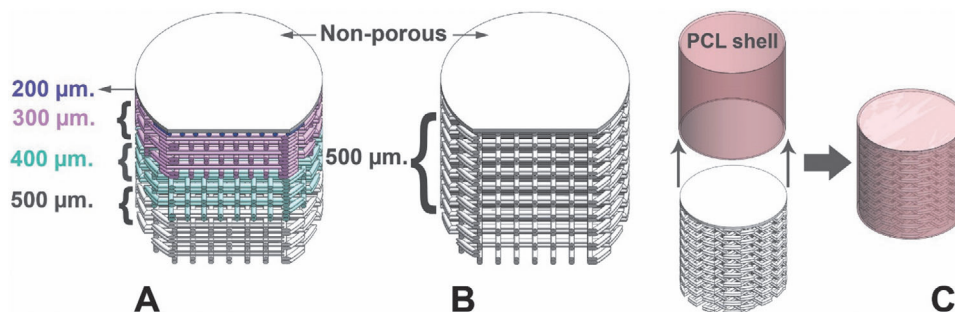
**Figure 1.** Schematic representation of the cross-section of the PCaP scaffolds with A) gradient and B) constant pore architecture. C) Representation of the PCL-encased PCaP scaffolds.
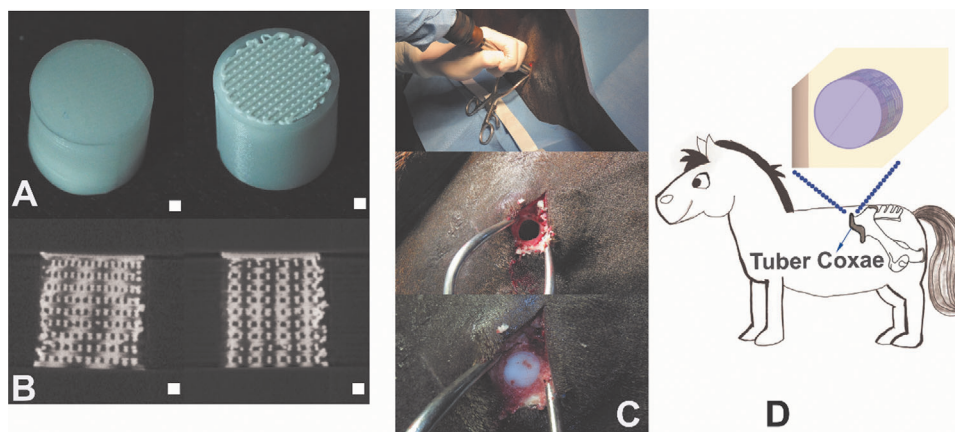


**Figure 2.** Visualization of the implant and surgical implantation procedure. A) Top (left) and bottom (right) view of the PCaP implants embedded into the PCL shell. B) Representative µCT images of an implant with gradient pore size (left) and constant pore size (right) before implantation. C) Sequence of implantation of the scaffolds in the tuber coxae, including drilling and exposure of the defect, followed by scaffold implantation. D) Schematic representation of the implant location in the tuber coxae. Scale bar = 1 mm.
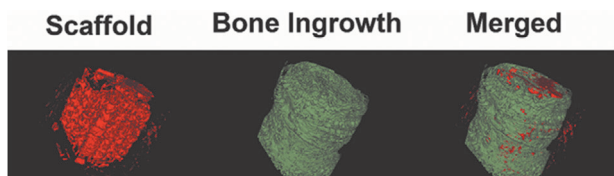


**Figure 3.** Formation of new bone throughout the whole volume of a constant porosity scaffold, as observed via µCT, in a sample in which the PCL cage was damaged and had permitted bone ingrowth from the side.

integrity of the PCL cage was compromised, new bone could readily invade the constructs, even resulting in a complete bridging of the defect (**Figure 3**). For the quantitative determination of neo-bone formation, the scaffolds were divided into three zones: zone 1 (basal part of PCaP scaffold); zone 2 (middle part of PCaP scaffold); and zone 3 (uppermost part of PCaP scaffold) (**Figure 4**A). The amount of new bone ingrowth in the constant porosity scaffold group ($85.13 \pm 34.62$ mm$^3$) was significantly larger than for the gradient scaffold group ($25.03 \pm 8.96$ mm$^3$) (Figure 4B). This difference was also evident in zones 1 (constant: $39.87 \pm 22.95$ mm$^3$; gradient: $13.68 \pm 1.18$ mm$^3$), 2 (constant: $26.16 \pm 8.19$ mm$^3$; gradient: $9.54 \pm 3.13$ mm$^3$), and zone 3 (constant: $19.13 \pm 7.36$ mm$^3$; gradient: $7.81 \pm 4.90$ mm$^3$) (Figure 4C). Additionally, the bone distribution in each printed layer varied, as a function of the distance to the scaffold-

native bone interface (basal side of the scaffold). In terms of ratio over the Volume of Interest (VOI), constant porosity scaffolds showed more bone volume (constant: $22.05 \pm 6.18\%$; gradient: $10.67 \pm 2.65\%$), as well as non-mineralized repair tissue (constant: $48.90 \pm 8.20\%$; gradient: $38,90 \pm 4.79\%$) (Figure 4D). The percentage of remaining ceramic material was significantly lower in the constant porosity group ($29.05 \pm 3.98\%$) than in the gradient group ($50.43 \pm 3.62\%$) (Figure 4D,E), suggesting a faster resorption of the material. Quantitative analysis of the total volume of ceramic before and after implantation (Figure 4E,F) from microcomputed tomography (µCT) data revealed an estimated percentage of scaffold degradation of $57.92 \pm 11.32\%$ for the constant scaffold group and of $33.47 \pm 8.67\%$ for the gradient scaffold.

3D reconstruction images from µCT data (**Figure 5**) showed the distribution of new bone formation in all scaffolds. The spatial distribution of the neo-tissue in the planes perpendicular to the longitudinal axis of the scaffold was analyzed in correspondence with the three main zones. Notably, new bone formation between the basal periphery and the transitional zone between zone 2 and zone 3 of the scaffold was more homogeneous in the constant scaffold than in the gradient scaffold. Bone formation appeared less uniform in zone 3 for both scaffold types, with the constant pore group having an overall considerably higher amount of neo-bone tissue.
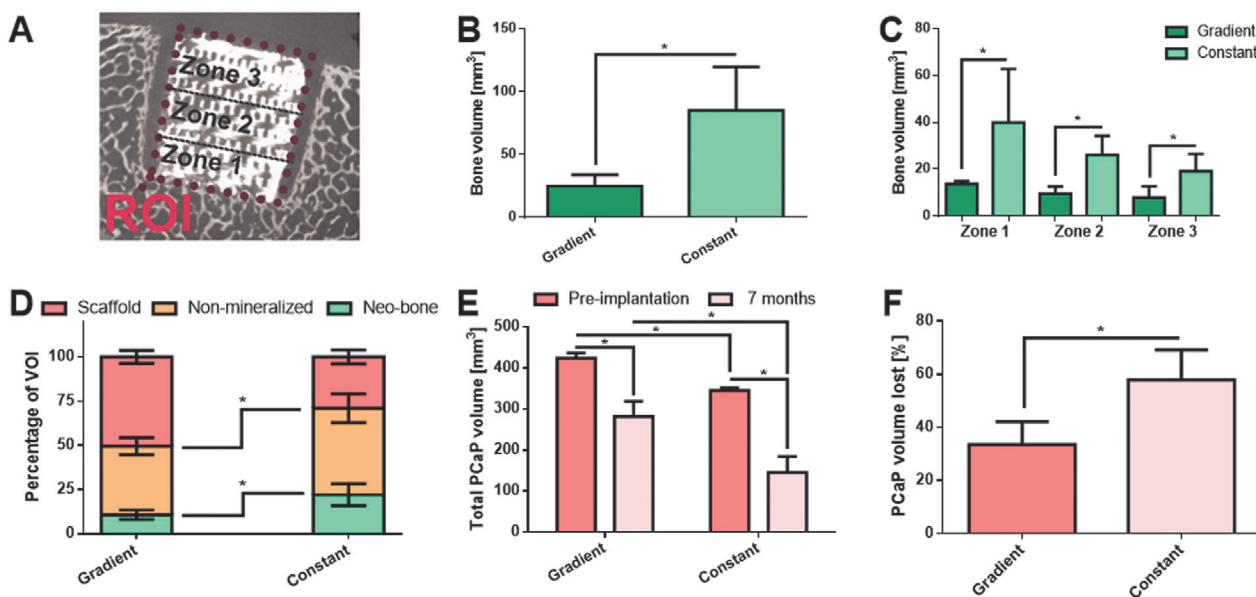
**Figure 4.** Quantitative analysis of bone regeneration, showing A) the three zones that were analyzed inside the scaffold; the quantification of new bone volume B) within the defect and C) within each zone, and D) ratio of the VOI occupied by new bone, non-mineralized tissue and remnants of PCaP scaffold after 7 months in vivo. E,F) Degradation of both types of scaffolds was highlighted by the quantification of the PCaP volume prior to implantation and at the end of the experiment. Asterisks indicate $p < 0.05$.
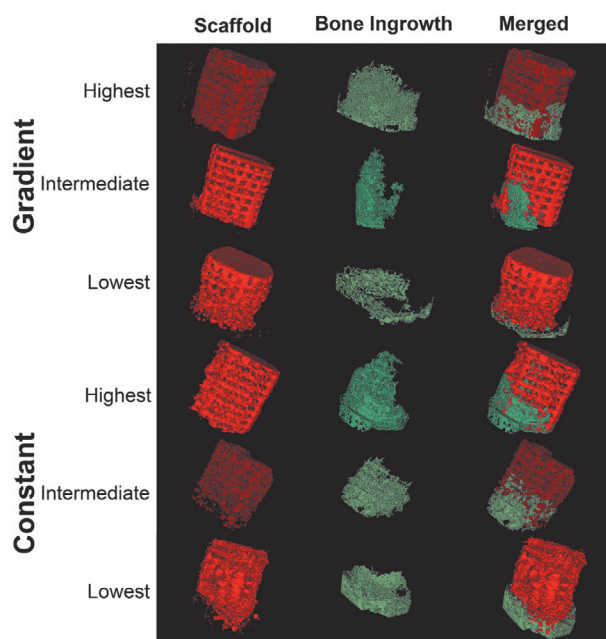


**Figure 5.** Representative µCT 3D reconstruction of the samples with highest, average, and lowest new bone formation in scaffolds with gradient and constant porosity in which the structural integrity of the PCL cage was preserved over the course of the experiment.

## 2.3. Histological Analysis of Cell Infiltration and New Bone and Vasculature Regeneration

### 2.3.1. Macroscopic Assessment

Once formalin-fixed samples were cut transversely, the positions of the implant were easily visible. From cross-sectional surface,
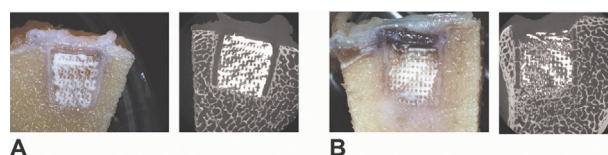


**Figure 6.** Representative cross-sections and µCT sectioned graphs of formalin-fixed samples showing appearance of both gradient A) and constant B) porous implants with surrounding tissue.

the PCL shells were visible in all samples as opaque white colored struts surrounding the area of the ceramic scaffold (**Figure 6**).

### 2.3.2. Microscopic Assessment of the Extent of Bone Healing

Microscopic analysis of the basic fuchsin and methylene blue stains of methyl methacrylate (MMA) embedded sections showed areas of new bone ingrowth within the macro-pores of the ceramic scaffolds in both gradient and constant scaffolds, displaying good attachment and integration between the neo-bone and the ceramic material (**Figure 7**A; Figure S2, Supporting Information). Histological analysis together with µCT images revealed the continuous connection between the host bone and the new bone ingrowth that penetrated into the scaffold from the host bone at the basal periphery of all scaffolds, regardless of the type of porosity, as well as the presence of non-calcified tissue, which was predominantly located in the regions of the scaffold further away from the interface with the native bone. The extent of new bone ingrowth varied per scaffold type. On the constant porosity scaffolds, new bone extended from the basal periphery of the scaffold, throughout the entire zone 2 to zone 3 (close to one side of the cylindrical wall) and toward the non-porous layer. In the gradient scaffolds, new bone extended to the middle region of zone 2 but not or hardly observed in zone 3. The newly formed
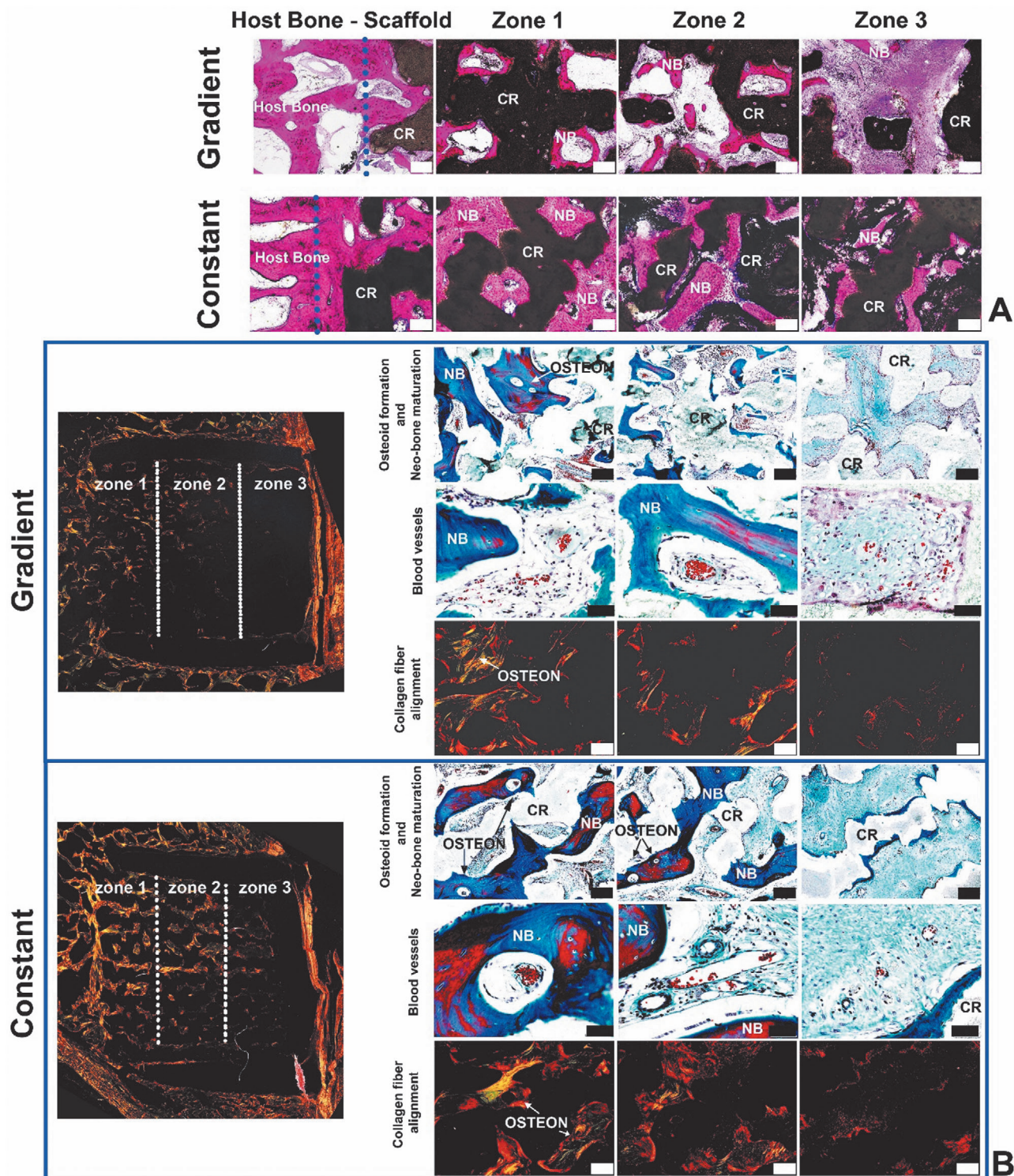
**ADVANCED
SCIENCE NEWS**

ww.advancedsciencenews.com

**ADVANCED
HEALTHCARE
MATERIALS**

www.advhealthmat.de



**Figure 7.** Histological assessment of neo-bone formation. A) Basic fuchsin and methylene blue stainings of undecalcified sections of both gradient and constant porous structures after 7 months of implantation showed connection between the original host bone and newly formed bone, as well as the presence of neo-bone ingrowth in a zone-dependent fashion, with the lowest amount of bone present in the third zone of the gradient scaffolds. (B; first row) Goldner's trichrome staining of decalcified sections of both gradient and constant porous structures after 7 months of implantation displayed mineralized newly formed bone (bluish-green color), and non-mineralized newly formed bone (red color). Newly formed bone with a lamellar pattern surrounding haversian canals could be observed (black/white arrows (osteon)) (Scale bar = 200 μm). (B; second row) Goldner's trichrome staining showing blood vessel formation in each zone (Scale bar = 50 μm). (B; third row) Picrosirius staining of decalcified sections when observed using polarized light microscopy showing birefringence of collagen fibers (Scale bar = 200 μm). CR = Ceramic Remnant, NB = New Bone.
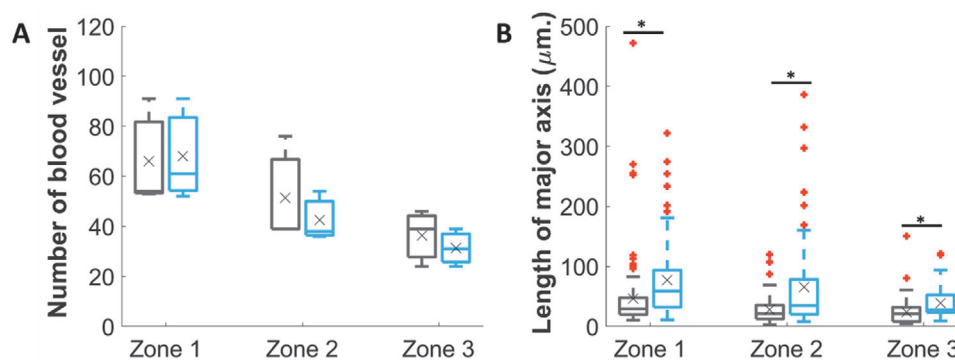
**1901807 (5 of 11)**

**ADVANCED
SCIENCE NEWS**
www.advancedsciencenews.com

**ADVANCED
HEALTHCARE
MATERIALS**
www.advhealthmat.de

**Figure 8.** Vascularization of neo-bone. A) Amount of blood vessels in each zone as observed from representative histological sections from both gradient and constant structure. B) Dimension of blood vessels in each zone based on length of the major axis. Central lines in each box of the boxplot indicate median, whereas the black X indicates average, and the red + indicate outliers. All data point, including the outliers were included in the statistical analysis, and * indicate $p < 0.05$ (grey box = gradient, blue box = constant).

bone inside the gradient porous scaffold was predominantly woven (immature) bone with some lamellar (mature) bone in zone 1 (Figure S3, Supporting Information). In the constant pore scaffolds both woven bone and lamellar bone were found, with a preponderance of lamellar bone, and found in higher amounts in all zones. Lamellar bone structures were found organized concentrically in a Haversian pattern around blood vessels, typical of native osteons (Figure 7B). New blood vessels from zone 1 to zone 3 in both constant and gradient scaffolds were prevalently located in newly formed lamellar bone and between the macropores of the ceramic printed structures. The number of blood vessels showed a (non-significant) decreasing trend from zone 1 to zone 3 in both architectures (**Figure 8**A). Regarding the dimension of the lumen, estimated by the length of the major axis, larger vessels were detected in the scaffolds with constant porosity (Figure 8B), across all zones. For gradient architectures, the sizes of blood vessels (mean ± SD) were: 46.60 ± 63.20 µm (zone 1), 27.95 ± 23.29 µm (zone 2), and 23.91 ± 21.74 µm (zone 3). For constant architectures, vessel sizes were: 77.53 ± 66.12 µm (zone 1), 65.39 ± 77.23 µm (zone 2), and 38.65 ± 26.58 µm (zone 3).

### 2.3.3. Microscopic Assessment: Cellular and Molecular Indicators of Bone Healing and Remodeling

All types of scaffold showed areas of non-calcified tissue infiltration with different volumes in each zone. At the site of new bone formation, there were areas with positive staining for osteonectin, a marker of osteocytes, and a fundamental component of the extracellular matrix, which was able to bind collagen and known to facilitate bone mineralization,[23] in indicating osteoblastic activity. Osteonectin-positive osteocytes were found embedded in lacunae inside newly formed mineralized bone osteons, and Tartrate-resistant acid phosphatase (TRAP) positive multinucleated cells were found in contact and in the proximity of the ceramic remnants, indicating osteoclastic activity that can mediate PCaP resorption (**Figure 9**; Figures S4–S6, Supporting Information).

In gradient structures, TRAP-positive multinucleated cells could be found throughout the scaffold from the basal periphery until zone 3, where they were found to be relatively higher

in number than in the constant pore structure (Figure S6A, Supporting Information). For both collagen type I and osteonectin (Figure S6B,C, Supporting Information), no significant difference could be detected between the gradient and constant porosity scaffolds, although areas with positive staining could be found mostly on the newly formed bone, which in the gradient structure was situated mostly in zone 1 and declined from there to zones 2 and 3.

## 3. Discussion

Native bone possesses a remarkable spontaneous regenerative ability, which is, however, not unlimited. Large bone defects caused by trauma, degenerative diseases, or tumor resection, as well as non-healing fractures, are common problems in musculoskeletal medicine and require new strategies and biomaterials to help unlock, restore, and guide bone repair. In this study, we investigated the long-term pro-regenerative performance of a new formulation of 3D-printed CaP-based bioceramic scaffolds in an in vivo equine model, as a function of the printed pore distribution.

All scaffolds showed the ability to promote neo-bone formation. Importantly, the incorporation and covalent crosslinking of the biodegradable poloxamer hydrogel, of which biocompatibility was previously demonstrated in vitro[24] and that ensured the printability and shape fidelity of the cement paste precursors, did not impede the healing process in vivo, and did not appear to provoke any detrimental inflammatory response. In both scaffold types, common features of the regenerative process can be identified. The volume within the pores of the scaffolds is filled with new bone and collagenous, non-calcified tissue. The latter is rich in osteonectin-positive cells, a marker of osteoblasts and a key matrix molecule for the initiation of the mineralization process.[25] This osteonectin abundance suggests the formation of an osteoid-like tissue, which is a preliminary step for the maturation toward neo-bone.[26] The amount of neo-bone and non-mineralized tissue differed between the gradient and the constant porosity scaffolds, with the latter displaying a significantly higher amount of both tissue types. This consistent difference in the degradation rate of the two architectures, albeit produced with
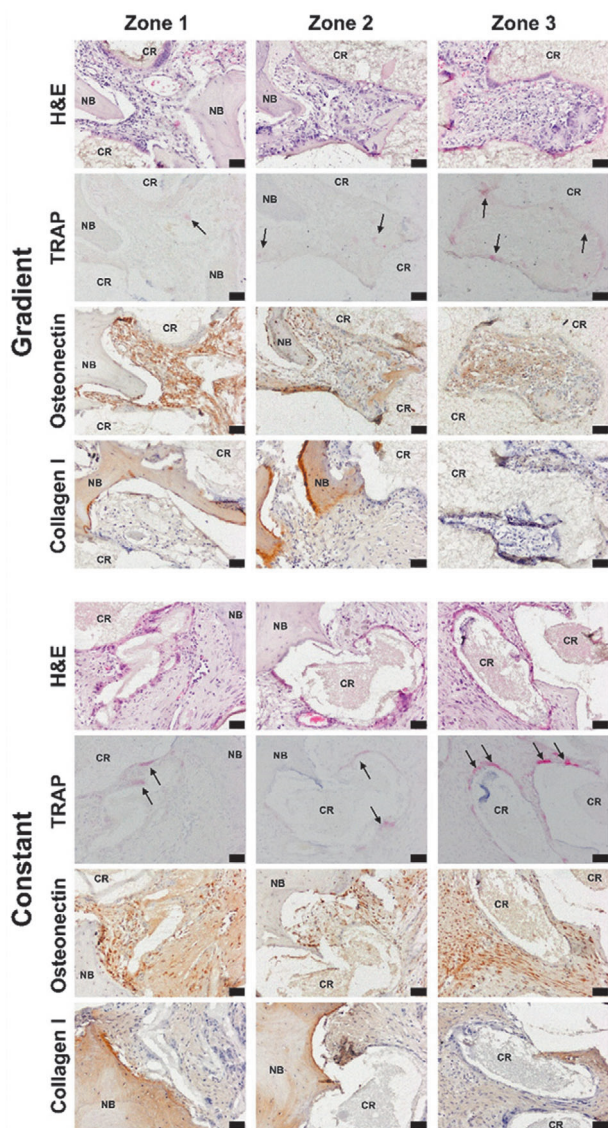
**Figure 9.** Hematoxylin and eosin (H&E), TRAP, osteonectin, and collagen type I staining of decalcified sections of both gradient and constant porous structures after 7 months of implantation. Positions of cells involved in new bone ingrowth were identified. TRAP-positive multinucleated cells were found lying against the surface of the ceramic material. Osteonectin-positive cells were present at the sites of apposition of newly formed bone and on the lining of newly formed bone. Osteocytes were embedded in the lacunae of the bone (Scale bar = 100 μm, CR = Ceramic Remnant, NB = New Bone).

the same materials, as well as its association with a difference in neo-bone deposition, suggests an active, cell-driven resorption. Indeed, there was ample osteoclast activity, as evidenced by the histological data (Figure S3, Supporting Information). Osteoclast activity was higher in the more remote zones of both scaffold types (zones 2 and 3), possibly indicating an ongoing more intense remodeling activity in those areas that are still in an early stage of neo-bone development.

Previous studies on CDHA and nano-HA, the main components of the PCaP scaffolds tested in this study, have convincingly shown their osteoconductive capacity.[14] Also, our work shows an osteoconductive component of the regenerative process, as neo-bone is progressing through the scaffold from the host tissue, and integrates tightly with the ceramic remnants, but our analysis at a single time point provides no clear evidence for intrinsic osteoinduction. In other studies, osteoinductive properties in the absence of exogenously added growth factors have already been demonstrated, first for nano-HA,[27] but also for CDHA, depending on the nanostructure of the biomimetic apatite particles resulting from the hardening process of the cement.[28] The superior performance of the constant porosity scaffolds as compared to the gradient group may not be intuitive. The gradient scaffolds do indeed present a lower degree of porosity, but all pores are well interconnected, with minimum size and geometry compatible with what is reported in the literature as necessary to permit bone ingrowth.[3,4,29]

In this study, the bone restorative process promoted by the 3D printed scaffolds was challenged by encasing the PCaP scaffolds in a PCL shell, to prevent infiltration of progenitor cells from the periosteum, and to facilitate only unidirectional bone ingrowth. However, in some occurrences (2/7 for both groups), the integrity of the PCL cage was lost over time, resulting in bone ingrowth also from the sides of the scaffolds. While these samples are still useful to estimate the osteoconductive potential of the material, this leads to an effective reduction of the sample size available to assess the effect of the porous architecture, although it did not compromise the overall analysis. To improve the consistency across donors, non-degradable materials should be recommended for future studies. Interestingly, this approach could possibly simulate features of large bone defects, as given the fact that bone growth can be conducted only from one side, distal regions on the defect have impaired interaction with the front of bone repair. While bones possess a remarkable ability to self-heal, especially concerning small defects, as new bone can infiltrate neighboring defects, large defects, areas toward the center of the scaffold and further away from the native bone have more difficulties in receiving all cells and signals necessary to trigger the regenerative process. In a previous study on the degradation and osteoconductive properties of $\alpha$- and $\beta$-Tricalcium phosphate, an 8mm-diameter titanium chamber was used to ensure equal space and prevent soft tissue interference.[30]

In the specific environment of this study, the overall design and architecture of the macro-pores greatly influenced the extent, quality, homogeneity, and spatial distribution of the new bone and of the repair tissue, in an anisotropic, region-dependent fashion. While for both the gradient and the constant architecture neo-bone was consistently well integrated with the native bone at the interface at the open side of the PCL cage, the constant pore diameter scaffolds exhibited significantly higher bone formation, as well as the presence of more mature lamellar bone over woven bone. This was seen already from zone 1, even though the macro-pore architecture in this region was the same for both gradient and constant constructs. Furthermore, in the constant group, the neo-bone was more homogenously distributed throughout the section of the scaffold in the plane parallel to the open face of the PCL shell, and these differences were also evident further away inside the scaffold, in zone 2. A similar trend could be observed for zone 3, although differences were not statistically significant for this zone. Overall, when also considering the bone forming

potential of the constructs including also the samples in which bone could infiltrate from the side of the scaffolds, the best extent of healing, that is, full bridging of the defect with bone present throughout the whole scaffold, was found only in the constant porosity group, possibly due to the larger pore size in all zones.

Vascularization is a critical step for bone regeneration.[31] Blood vessels, associated with bone (either lamellar, as Haversian canals, or woven) and non-mineralized tissue, were present throughout all zones, regardless of the architecture. The size of these vessels, which is an indicator of vessel stability and vascularization potential of the scaffolds,[32] showed a decreasing trend from zone 1 to zone 3 for both architectures, albeit this difference was not statistically significant. However, there was a significant difference in size, with larger average lumen size for the vessels in the constant porosity group, when comparing the effect of the pore architecture within a given zone. Vascular infiltration is a necessary element for bone tissue remodeling and the degree of maturation and amount of blood vessels (Figure 8) can affect the influx of nutrients, biochemical cues, and cells (i.e., osteoclasts, progenitor cells and osteoblasts) that accelerate neo-bone deposition and development.[33,34] The decrease in the maturity and size of blood vessels from the constant to the gradient scaffolds seems correlated with our findings for neo-bone formation, which was consistently better for the constant group regardless of the zone.

Importantly, our results suggest that areas further away from the front of mineralization may influence other regions. This is particularly relevant, as areas with poor regeneration may limit osteoconductive repair also in regions close to the native bone. In the constant group, vascularization and repair tissue can progress with relative more ease from zone 1 to 2 (and finally to 3), compared to the gradient group, leading to faster degradation and remodeling of the scaffold, accompanied by a satisfactory regeneration of bone in zones 1 and 2. Conversely, in gradient scaffolds, the hindrance of neo-bone progression in the deeper zones also negatively affects the quality and kinetics of the remodeling of the repair tissue in the first zone. Although such phenomena might not be experienced in a relatively small scaffold in which the porous architecture is accessible from all sides, this would be relevant for large scaffolds and the observation may hence be important for bone scaffold design and especially scaling-up of these scaffolds.

Finally, in the perspective of scaling up bone regenerative scaffolds, the selection of appropriate animal models is fundamental. Most biomaterials for bone regeneration are tested in small animal models, which possess superior regenerative ability compared to humans and larger animals.[35] While these models provide important information on the osteoconductive and osteoinductive properties of a material, they poorly represent the human musculoskeletal milieu and the associated mechanical loads. Therefore, they are insufficient to translate new biomaterials toward human and veterinary clinical practice. The model proposed in this study may aid significantly toward this objective. A previous study on osteoinductive gelatin/$\beta$-TCP sponges demonstrated favorable bone regeneration in third metacarpal bone defects in horses.[36] This location of defect is, however, challenging in terms of surgical approach and interventions at this site easily lead to severe discomfort of the animals, which will manifest as lameness. The equine tuber coxae has not previously been used as a site for bone regeneration studies thus far, but presents several advantages: it is easily accessible, contains compact and trabecular bone, is hardly affected by skin displacement, and surgery can be performed in the standing horse The little impact of surgical interventions at this site also allows the simultaneous investigation of novel regenerative approaches at different sites (e.g., stifle joints for cartilage repair); thus, contributing to the refinement and reduction of experimental animal use, in compliance with the 3R principle.[37] Apart from all practical advantages that have been discussed earlier and different to most other large animals, such as sheep and goats,[38] horses are often also orthopedic patients, and thus may profit from the outcome of this type of experiments.

## 4. Conclusion

In this work, the long-term in vivo performance of 3D-printed porous PCaP based scaffolds with different pore distributions (vertical gradient and constant porosity) was tested in an equine orthotopic bone defect model. The challenging environment created by PCL capping provided valuable insights in the influence of scaffold pore architecture on bone neo-formation, although replacing PCL for non-degradable materials is recommended. In this setting, the macro-pore patterns of the scaffolds, which were produced from compositionally equivalent material, were shown to both influence new bone ingrowth and material degradation. This is important information for scaffold manufacturing, especially with regard to the possible upscaling of scaffolds for healing of larger bone defects. This study has further shown that the –porosity-influenced- bone ingrowth and vascular characteristics in turn have an effect on bone formation and/or scaffold degradation at places at a relatively large distance from the interfaces of the scaffold with the native bone. Additionally, the study highlights the value of the equine tuber coxae model for orthotopic testing of bone scaffolds. The tuber coxae is situated at the end of the wing of the ileum and hence is part of the pelvis. It is a place where muscles attach, such as the tensor fasciae latae muscle. It contains mainly trabecular bone, which is surrounded, however, by a rather thin layer of cortical bone. This is not unlike the situation in a joint where the subchondral bone is made up of trabecular bone that is shielded from the articular cartilage by the subchondral bone plate. Apart from many advantages including ease of surgery, maximum size of implants, and limited experimental animal welfare impact, there is the important ethical consideration that for orthopedic regenerative medicine studies, the horse is not merely an experimental animal, but a target species in its own right that may benefit from possible positive outcomes of experimental studies.

## 5. Experimental Section

*PCaP Paste Preparation*:  PCaP paste was prepared by mixing a powder particle phase and a liquid phase. Briefly, the optimal distribution of the particles and liquid phases that allowed the paste to be printable was 70% and 30% w/w, respectively. The powder consisted of microparticles of milled $\alpha$-TCP (average size 3.37 μm, Cambioceramics, The Netherlands) mixed with 4% w/w nano-HA (average size 200 nm, Sigma-Aldrich). The liquid phase consisted of a shear-thinning

**ADVANCED
SCIENCE NEWS**
www.advancedsciencenews.com

**ADVANCED
HEALTHCARE
MATERIALS**
www.advhealthmat.de

hydrogel precursor solution dissolved in phosphate-buffered saline (PBS), supplemented with ammonium persulphate (APS, Sigma Aldrich, 25 mм), to form a 40% (w/v) solution. The dissolved polymer, forming this hydrogel precursor, consisted of a biodegradable and crosslinkable poloxamer derivative (P-CL-MA), which was custom synthesized by grafting a biodegradable $\epsilon$-caprolactone ester block and a methacrylate group onto both terminal hydroxyl groups of poloxamer 407 (Sigma-Aldrich), as previously described.[24] Before mixing, the powder and liquid phases were stored separately at 4 °C for 30 min and finally the P-CL-MA solution was added to a composite solid particle at 4 °C and manually mixed with a spatula. To ensure homogeneous distribution of solid particles, the mixing process was performed for 3 min at 4 °C. Finally, the PCaP paste was loaded into a 5 mL dispensing cartridge, closed with retainer caps, and stored at 4 °C until using.

*Porous PCaP Scaffold Preparation*: Cylindrical PCaP scaffolds (diameter: 9.8 mm. height: 9.5 mm) were designed and produced using a pneumatic extrusion printer (RegenHU, Villaz-St-Pierre, Switzerland). Scaffold architecture was designed and converted to printing path and eventually g-code with the BioCAD software (RegenHU, Villaz-St-Pierre, Switzerland). The PCaP paste was extruded through a conical nozzle (inner diameter = 250 μm, pressure = 0.21 MPa, translation speed 2 mm·s$^{-1}$ and layer height of 250 μm) at ambient temperature (20–25 °C). All scaffolds were printed with a 0–0–90–90° laydown pattern, stacking two contiguous layers in the same direction in order to ensure a constant lateral porosity of 500 μm. Two types of axial pore structures (Figure 1) were formed: i) a gradient of porosity with a discrete four-step reduction of the strand-to-strand distance (500, 400, 300, and 200 μm), and ii) a constant pore pattern, created by printing within each layer PCaP filaments with a strand-to-strand distance of 500 μm. For both types of scaffolds, a non-porous last layer was printed on top. After finishing the printing process, PCaP scaffolds were set by leaving them in a humidified environment, saturated with water vapor at 37 °C for three days. Subsequently, the scaffolds were immersed in tetramethylethylenediamine (TEMED, Life Technologies, 25 mм) solution in PBS at 37 °C for 1 h, to allow the polymerization of the P-MA component of the PCaP cement, initiated by TEMED diffusing into the APS-enriched cement formulation. As observed with x-ray diffraction (XRD) analysis, about 95.8% of the cement precursor was converted to poorly crystalline CDHA after setting and polymer crosslinking,[39] Crosslinked scaffolds were rinsed and washed with PBS twice, dried in air at ambient temperature, and stored until further use. The overall range of porosity as measured via μCT was found to be 40.03 ± 1.78% and 51.14 ± 0.78% for the constant and gradient structure, respectively. The mechanical properties were characterized by performing an unconfined compression tests (MTS criterion Electromechanical Universal Test Systems, model 42, 500 N load cell). Samples were kept in PBS for at least 30 min before performing the test. The testing system was set to apply displacement ramp (0.5 mm min$^{-1}$) until failure of the structure. The tangent modulus, calculated in the elastic regime and the ultimate strength, was found to be 105.80 ± 55.74 and 1.36 ± 0.59 MPa, respectively for the constant scaffold, and of 208.37 ± 84.90 and 3.09 ± 1.17 MPa for the gradient structures, in line with what previously observed.[39]

*PCL Cylindrical Shell, Implant Assembly, and Sterilization*: To allow tissue growth into the construct from a single direction, the entire scaffold, except for the side that was positioned towards the bottom of the osteal defect, was insulated with a 3D-printed bucket-shaped medical-grade PCL (Purasorb PC 12 Corbion PURAC, The Netherlands, with printing temperature of 80 °C, translation speed 1 mm·s$^{-1}$, and layer thickness of 200 μm)) shell (height: 10 mm, inner diameter: 10 mm, outer diameter: 10.47 mm) by using the same pneumatic-driven printer as described for the PCaP paste. Hardened and crosslinked PCaP scaffolds were pressed-fit inside the PCL shell, with the non-porous PCaP layer at the closed side of the shell (Figure 1). All assembled scaffolds were sterilized by gamma irradiation (8kGy) and kept separately in sterile falcon tubes until implantation.

*In Vivo Study Design and Surgical Procedure*: Cylindrical defects were drilled into the tuber coxae of the ilium in eight horses (one defect per side) (Figure 2). Each horse received both one gradient and one constant porous scaffold (with random left/right distribution). Scaffolds were placed by letting the open circular side of the PCL cylindrical shell in contact with native

bone at the bottom of the defect while the closed circular side was covered with periosteum. The protocols and studies described were approved by the ethical and animal welfare committees of the National University of Costa Rica. Eight healthy adult Criollo breed horses (mean age 7.1 years, range 5–9 years; mean weight 319 kg, range 275–375 kg) were used. The study was performed on a cohort of horses which were already involved in another study, in which engineered constructs were implanted in osteochondral defects in the stifle joint. As there is no cross-talk between the two anatomical locations (stifle and tuber coxae), the tuber coxae bone defect is a suitable model to perform multiple parallel assays, minimizing the need of experimental animals, in accordance to the 3Rs principle (reduce, refine, replace). Horses were clinically sound on lameness examination and did not have clinical or radiographic evidence of joint pathology. They were housed in individual box stalls and fed a standard maintenance ration of concentrate with hay ad libitum and had free access to water during the first three months of the study, in order to avoid excessive loads on the stifle joint, in relation to the scaffolds implantation in the osteochondral defect. After this period, they had free exercise at pasture at the University farm, with unlimited access to hay and water. After premedication with xylazine ((Pisa, Mexico), 1.1 mg kg$^{-1}$, intravenous (IV)), anesthesia was induced with midazolam ((Holliday, Argentina), 0.05 mg kg$^{-1}$, IV) and ketamine ((Holliday, Argentina), 2.2 mg kg$^{-1}$, IV). Afterward, the horse was positioned in lateral recumbency. General anesthesia was maintained with isoflurane in oxygen. An incision was made in the skin and subcutaneous tissue 10 cm above the tuber coxae to expose the underlying bone. Once the tuber coxae was exposed, a cylindrical microdefect of 11 mm wide x 10 mm deep was created using a power drill. Defect sites were flushed with saline (Baxter, USA) and the experimental scaffolds were implanted using a press-fit approach. Subcutaneous tissue and skin were sutured, and the horses were allowed to recover without wound dressings.

*Post-Operative Care and Monitoring*: Horses received antibiotics for 5 days (procaine penicillin (Phenix, Belgium), 15 000 IU kg$^{-1}$, intramuscular (IM), once daily (SID) and gentamicin (KEPRO BV, the Netherlands), 6.6 mg kg$^{-1}$, IV, SID), and non-steroidal anti-inflammatory drugs (phenylbutazone (Lisan, Costa Rica), 2.2 mg kg$^{-1}$, oral administration (PO), twice daily (BID)) during the first 10 days. Horses were clinically monitored daily for rectal temperature, heart rate, and respiratory rate, as well as stance, demeanor, and general appearance. The surgical wounds were inspected, and the area gently palpated for local heat, swelling, and tenderness. Locomotion was evaluated daily at walk and horses were occasionally trotted up to check for eventual subtle lameness. Routine blood analysis (complete blood count (CBC), chemistry panel) was performed at months 1, 3, and 6 post-operatively. From 3 months post-operation, horses were turned out into pasture, allowing free exercise until the end of the experiment.

*Euthanasia and Sample Harvesting*: One horse was euthanized because of an accident at pasture unrelated to the study at 4 months postoperatively and was excluded from the study. The remaining seven horses were euthanized 7 months post-operatively. Deep anesthesia was induced with a combination of xylazine ((Pisa, Mexico), 1 mg kg$^{-1}$, IV) followed by ketamine and midazolam ((Holliday, Argentina), 3 mg kg$^{-1}$, IV and 0.05 mg kg$^{-1}$, IV, respectively), after which a bolus of oversaturated magnesium sulfate (200 g L$^{-1}$) and chloral hydrate (200 g L$^{-1}$) solution was administered IV to effect. Death was confirmed by absence of breathing, ictus and corneal reflex. After dissection of the skin and subcutaneous tissues, the tuber coxae was exposed and the surgical sites were readily recognizable. Macroscopic pictures were taken and blocks of tissue containing the defects were excised. Pieces containing the defects were fixed and stored in formalin in individual plastic containers.

*μ-CT Evaluation*: Three assembled implants of either constant or gradient porous PCaP scaffolds were randomly selected for scanning in a μ-CT scanner (Quantum FX-Perkin Elmer) before implantation. All formalin-fixed tissue explants, containing the implant and the surrounding native tissue that were harvested postmortem at the endpoint of an experiment, were also scanned (voltage = 90 kV, current = 200 μA, voxel size = 20 μm³, and total scanning time = 3 min). Subsequently, the 3D reconstructed images were processed and analyzed using image J[40] and Bone J[41] software, respectively. First, a two-dimensional (2D) region of

**ADVANCED
SCIENCE NEWS**

www.advancedsciencenews.com

**ADVANCED
HEALTHCARE
MATERIALS**

www.advhealthmat.de

interest (ROI) was selected in a transverse plane (parallel to the surface of the scaffold) at the boundary between the ceramic scaffold and the inner wall of the PCL chamber. For the analysis of the whole construct, similar ROIs were created every two stacks (512 stacks/each µCT file), then a 3D VOI was obtained by automatically interpolating these ROIs in ImageJ. For the quantification by separating into three zones, a similar process was followed, except that three VOIs were identified. Subsequently, thresholding was performed in order to select either the signal derived from the ceramic scaffold only, or from the newly formed bone. Finally, the volume fraction within a given VOI was analyzed using the Bone J plugin in ImageJ. Seven main parameters were quantified including total volume of newly formed bone in the overall VOI, volume of newly formed bone in each zonal VOI, percentage of new bone ingrowth ((new bone volume/VOI) * 100), percentage of remaining PCaP ((volume of ceramic/VOI) * 100), estimated percentage of other, non-mineralized tissue infiltration (100 − (percentage of new bone ingrowth + percentage of remaining ceramic)), total volume of ceramic material of scaffolds before and after implantation, and percentage of PCaP volume loss. µ-CT 3D reconstructions of new bone formation and remaining ceramic were generated using the 3D Slicer software (4.10.0, BWH and 3D Slicer contributors).

*Histological Assessment*: After retrieval, all formalin-fixed samples were kept in formalin (4%) and cut through the defect area and, therefore, longitudinally through the scaffold to obtain two rectangular cross sections for embedding in either paraffin or MMA resin. For paraffin embedding, tissue explants were decalcified with ethylenediaminetetraacetic acid (EDTA) disodium salt (0.5 м) for 6 weeks. Dehydration was performed through a graded ethanol series, followed by clearing in xylene and embedding in paraffin. Embedded samples were sectioned into 5 µm thin slices. To observe the morphology of cells that had infiltrated in the porous constructs, H&E staining was performed (nuclei: blue, other parts: pink). Subsequently, to understand the identity of specific cell populations found within the scaffolds, different stainings to detect cells involved in bone remodeling were performed. TRAP stain was performed to reveal TRAP-positive osteoclasts (showing in red). Stainings for osteonectin, a major non-collagenous protein in bone, (Osteonectin AB SPARC AON-1, DSHB; nuclei: blue, positive osteonectin: brown) and for collagen type I, (Anti-collagen I antibody EPR7785, Abcam; nuclei: blue, positive collagen type I: brown) were performed to reveal the activity of osteoblasts. To assess the presence of collagen fibers within the newly formed bone and to differentiate between non-mineralized (osteoid) and mineralized bone, Goldner's trichrome stain was performed (nuclei: blue, immature bone: red orange, mineralized mature bone: blue green). To observe the spatial arrangement of collagen fibers in the repair tissue, a picrosirius red stain was performed and imaged under polarized light which revealed collagen birefringence (collagen: birefringent patterns against a black background). For MMA embedding, formalin-fixed tissue sections were dehydrated through a graded ethanol series, embedded in MMA resin and allowed to harden at 37 °C in a water bath overnight. Embedded samples were sectioned into 330 µm-thick slices. Thereafter, all sections were stained with basic fuchsin and methylene blue to visualize new bone ingrowth and soft tissue infiltration (nuclei: blue, pink: bone). Stained histological slides were imaged using a light microscope (Olympus BX51, Olympus Nederland B.V.) equipped with a digital camera (Olympus DP73, Olympus Nederland B.V.). Also, for the analysis of the histological data, the implant region was divided into three zones that were dependent on the distance across the depth of the scaffold, starting from the native bone-scaffold interface. Relative amounts of TRAP-positive stain, osteonectin-positive stain, and collagen type I-positive stain were quantified, converting the acquired microscopy images to binary files, applying a threshold to select the stained area and quantifying the area coverage of the staining (ratio between the stained area and the total area of new tissue formation (excluding the ceramic). The size and number of blood vessels penetrating into the scaffolds were also quantified by selecting three random pictures from each zone of the scaffolds and counting the number of vessels and measuring the length of their main axis with ImageJ software.

*Statistical Analysis*: Measurements at the endpoint of the in vivo experiment were performed on seven horses (N = 7). Regarding the analysis of the effect of the printed pore structure, three samples from each group were withdrawn from the evaluation, either because the structural integrity of the PCL cage was found to be compromised, with neo-bone infiltrating from the sides of the structure, or due to failure to retrieve the entirety of the scaffold (final sample size N = 4 for both groups). Calculated values for the constant and gradient porosity scaffolds were reported as mean ± standard deviation. Statistical analysis was performed using Matlab (R2018a, The MathWorks, Inc.). A Mann–Whitney U-test was performed to investigate the differences between the groups in terms of total bone volume, zonal bone volume, percentage of PCaP volume loss, including size and number of blood vessels. Likewise, the same test was used for evaluating the bone volume fraction, remaining material volume fraction, and non-mineralized tissue volume fraction in the VOI. Two-way ANOVA was performed for analyzing the total PCaP volume before and after implantation. Statistical significance was considered for $p < 0.05$.

## Conflict of Interest

The authors declare no conflict of interest.

[1] J. J. Li, M. Ebied, J. Xu, H. Zreiqat, *Adv. Healthcare Mater.* **2018**, *7*, 1701061.
[2] S. Samavedi, A. R. Whittington, A. S. Goldstein, *Acta Biomater.* **2013**, *9*, 8037.
[3] V. Karageorgiou, D. Kaplan, *Biomaterials* **2005**, *26*, 5474.
[4] Q. L. Loh, C. Choong, *Tissue Eng., Part B* **2013**, *19*, 485.
[5] B. D. Ratner, *Regener. Biomater.* **2016**, *3*, 107.
[6] I. R. Serra, R. Fradique, M. C. S. Vallejo, T. R. Correia, S. P. Miguel, I. J. Correia, *Mater. Sci. Eng., C* **2015**, *55*, 592.
[7] A. Di Luca, I. Lorenzo-Moldero, C. Mota, A. Lepedda, D. Auhl, C. Van Blitterswijk, L. Moroni, *Adv. Healthcare Mater.* **2016**, *5*, 1753.
[8] S. Cai, J. Xi, C. K. Chua, *Methods Mol. Biol. (N. Y.)* **2012**, *868*, 45.
[9] S. Yin, W. Zhang, Z. Zhang, X. Jiang, *Adv. Healthcare Mater.* **2019**, *8*, 1801433.

[10] R. A. Perez, M.-P. Ginebra, *J. Mater. Sci.: Mater. Med* **2013**, *24*, 381.

[11] J. Groll, J. A. Burdick, D. W. Cho, B. Derby, M. Gelinsky, S. C. Heilshorn, T. Jüngst, J. Malda, V. A. Mironov, K. Nakayama, A. Ovsianikov, W. Sun, S. Takeuchi, J. J. Yoo, T. B. F. Woodfield, *Biofabrication* **2018**, *11*, 013001.

[12] T. Ahlfeld, F. Doberenz, D. Kilian, C. Vater, P. Korn, G. Lauer, A. Lode, M. Gelinsky, *Biofabrication* **2018**, *10*, 045002.

[13] A. R. Akkineni, Y. Luo, M. Schumacher, B. Nies, A. Lode, M. Gelinsky, *Acta Biomater.* **2015**, *27*, 264.

[14] A. Barba, Y. Maazouz, A. Diez-Escudero, K. Rappe, M. Espanol, E. B. Montufar, C. Öhman-Mägi, C. Persson, P. Fontecha, M.-C. Manzanares, J. Franch, M.-P. Ginebra, *Acta Biomater.* **2018**, *79*, 135.

[15] A. I. Pearce, R. G. Richards, S. Milz, E. Schneider, S. G. Pearce, *Eur. Cells Mater.* **2007**, *13*, 1.

[16] C. J. Moran, A. Ramesh, P. A. J. Brama, J. M. O'Byrne, F. J. O'Brien, T. J. Levingstone, *J. Experiment. Orthopaed.* **2016**, *3*, 1.

[17] C. Gyles, *Can Vet J* **2016**, *57*, 345.

[18] P. J. Cope, K. Ourradi, Y. Li, M. Sharif, *Osteoarthritis and Cartilage* **2019**, *27*, 230.

[19] E. L. Kuyinu, G. Narayanan, L. S. Nair, C. T. Laurencin, *J Orthop Surg Res* **2016**, *19*, 3.

[20] R. B. Williams, L. S. Harkins, C. J. Hammond, J. L. N. Wood, *Equine Veterinary J.* **2001**, *33*, 478.

[21] A. Bigham-Sadegh, A. Oryan, *Connect. Tissue Res.* **2015**, *56*, 175.

[22] I. M. Wright, *Equine Veterinary Education* **2017**, *29*, 391.

[23] J. D. Termine, H. K. Kleinman, S. W. Whitson, K. M. Conn, M. L. McGarvey, G. R. Martin, *Cell* **1981**, *26*, 99.

[24] F. P. W. Melchels, M. M. Blokzijl, R. Levato, Q. C. Peiffer, M. de Ruijter, W. E. Hennink, T. Vermonden, J. Malda, *Biofabrication* **2016**, *8*, 035004.

[25] E. M. Rosset, A. D. Bradshaw, *Matrix Biol.* **2016**, *52–54*, 78.

[26] P. Gehron Robey, Chapter 17, *Noncollagenous Bone Matrix Proteins*, 3rd edition (Eds: J. P. Bilezikian, L. G. Raisz, T. J. Martin), Academic, San Diego, USA **2008**, p. 335.

[27] J. Hu, Y. Zhou, L. Huang, J. Liu, H. Lu, *BMC Musculoskeletal Disord.* **2014**, *15*, 114.

[28] A. Barba, A. Diez-Escudero, Y. Maazouz, K. Rappe, M. Espanol, E. B. Montufar, M. Bonany, J. M. Sadowska, J. Guillem-Marti, C. Öhman-Mägi, C. Persson, M.-C. Manzanares, J. Franch, M.-P. Ginebra, *ACS Appl. Mater. Interfaces* **2017**, *9*, 41722.

[29] A. Marrella, T. Y. Lee, D. H. Lee, S. Karuthedom, D. Syla, A. Chawla, A. Khademhosseini, H. L. Jang, *Mater. Today* **2018**, *21*, 362.

[30] M. Yamada, M. Shiota, Y. Yamashita, S. Kasugai, *J. Biomed. Mater. Res., Part B* **2007**, *82B*, 139.

[31] J. R. García, A. J. García, *Drug Delivery Transl. Res.* **2016**, *6*, 77.

[32] S. Scaglione, C. Ilengo, M. Fato, R. Quarto, *Tissue Eng., Part A* **2009**, *15*, 155.

[33] J. Filipowska, K. A. Tomaszewski, Ł. Niedźwiedzki, J. A. Walocha, T. Niedźwiedzki, *Angiogenesis* **2017**, *20*, 291.

[34] A. Malhotra, P. Habibovic, *Trends Biotechnol.* **2016**, *34*, 983.

[35] G. F. Muschler, V. P. Raut, T. E. Patterson, J. C. Wenke, J. O. Hollinger, *Tissue Eng., Part B* **2010**, *16*, 123.

[36] N. Tsuzuki, K. Otsuka, J. Seo, K. Yamada, S. Haneda, H. Furuoka, Y. Tabata, N. Sasaki, *Res. Veterinary Sci.* **2012**, *93*, 1021.

[37] F. Guhad, *J. Am. Assoc. Lab. Anim. Sci* **2005**, *44*, 58.

[38] L. D. Loozen, Y. J. M. van der Helm, F. C. Öner, W. J. A. Dhert, M. C. Kruyt, J. Alblas, *Tissue Eng., Part A* **2015**, *21*, 1672.

[39] P. Diloksumpan, M. de Ruijter, M. Castilho, U. Gburech, T. Vermonden, P. R. van Weeren, J. Malda, R. Levato, *Biofabrication* **2020**, *12*, 025014.

[40] J. Schindelin, I. Arganda-Carreras, E. Frise, V. Kaynig, M. Longair, T. Pietzsch, S. Preibisch, C. Rueden, S. Saalfeld, B. Schmid, J.-Y. Tinevez, D. J. White, V. Hartenstein, K. Eliceiri, P. Tomancak, A. Cardona, *Nat. Methods* **2012**, *9*, 676.

[41] M. Doube, M. M. Kłosowski, I. Arganda-Carreras, F. P. Cordelières, R. P. Dougherty, J. S. Jackson, B. Schmid, J. R. Hutchinson, S. J. Shefelbine, *Bone* **2010**, *47*, 1076.